Mediterranean winter rainfall in phase with African monsoon during past 1.36 million years

Bernd Wagner[1]*†, Hendrik Vogel[2]†, Alexander Francke[1,3], Tobias Friedrich[4], Timme Donders[5], Jack H. Lacey[6], Melanie J. Leng[6,7], Eleonora Regattieri[8,9], Laura Sadori[10], Thomas Wilke[11], Giovanni Zanchetta[8], Christian Albrecht[11], Adele Bertini[12], Nathalie Combourieu-Nebout[13], Aleksandra Cvetkoska[5, 11], Biagio Giaccio[14], Andon Grazhdani[15], Torsten Hauffe[11], Jens Holtvoeth[16], Sebastien Joannin[17], Elena Jovanovska[11], Janna Just[1,18], Katerina Kouli[19], Ilias Kousis[20], Andreas Koutsodendris[20], Sebastian Krastel[21], Niklas Leicher[1], Zlatko Levkov[22], Katja Lindhorst[21], Alessia Masi[10], Martin Melles[1], Anna M. Mercuri[23], Sebastien Nomade[24], Norbert Nowaczyk[25], Konstantinos Panagiotopoulos[1], Odile Peyron[17], Jane M. Reed[26], Leonardo Sagnotti[27], Gaia Sinopoli[10], Björn Stelbrink[11], Roberto Sulpizio[28, 29], Axel Timmermann[30,31], Slavica Tofilovska[22], Paola Torri[32], Friederike Wagner-Cremer[5], Thomas Wonik[33], Xiaosen Zhang[34]

[1]Institute of Geology and Mineralogy, University of Cologne, Cologne, Germany.

[2]Institute of Geological Sciences & Oeschger Centre for Climate Change Research, University of Bern, Bern, Switzerland.

[3]School of Earth, Atmospheric, and Life Science, University of Wollongong, Wollongong, Australia.

[4]International Pacific Research Center, University of Hawaii at Manoa, Honolulu, Hawaii, USA.

[5]Palaeoecology, Department of Physical Geography, Utrecht University, Utrecht, The Netherlands.

[6]National Environmental Isotope Facility, British Geological Survey, Nottingham, UK.

[7]Centre for Environmental Geochemistry, School of Biosciences, University of Nottingham, UK.

[8]Dipartimento di Scienze della Terra, University of Pisa, Pisa, Italy.

[9]Institute of Earth Sciences and Earth Resources-Italian National Research Council (IGG-CNR), Pisa, Italy.

[10]Dipartimento di Biologia Ambientale, Università di Roma "La Sapienza", Rome, Italy.

[11]Department of Animal Ecology & Systematics, Justus Liebig University Giessen, Giessen, Germany.

[12]Dipartimento di Scienze della Terra, Università di Firenze, Firenze, Italy.

[13]CNRS UMR 7194, Muséum National d'Histoire Naturelle, Institut de Paléontologie Humaine, Paris, France.

[14]Istituto di Geologia Ambientale e Geoingegneria – CNR, Rome, Italy.

[15]Faculty of Geology and Mineralogy, University of Tirana, Albania.

[16]School of Chemistry, University of Bristol, Bristol, UK.

[17]CNRS UMR 5554, Institut des Sciences de l'Evolution de Montpellier, Université de Montpellier, Montpellier, France.

[18]Fachbereich Geowissenschaften, Universität Bremen, Bremen, Germany.

[19]Faculty of Geology and Geoenvironment, National and Kapodistrian University of Athens, Athens, Greece.

[20]Paleoenvironmental Dynamics Group, Institute of Earth Sciences, Heidelberg University, Heidelberg, Germany.

[21]Institute of Geosciences, Christian-Albrechts-Universität zu Kiel, Kiel, Germany.

[22]University Ss Cyril and Methodius, Institute of Biology, Skopje, FYROM.

[23]Dipartimento di Scienze della Vita, Laboratorio di Palinologia e Paleobotanica, Università di Modena e Reggio Emilia, Modena, Italy.

[24]Laboratoire des Sciences du Climat et de l'Environnement, UMR 8212, CEA/CNRS/UVSQ et Université Paris-Saclay, Gif-Sur-Yvette, France.

[25]Helmholtz Centre Potsdam, GFZ German Research Centre for Geosciences, Potsdam, Germany.

[26] The Department of Geography, Geology and Environment, University of Hull, Hull, UK.

[27]Istituto Nazionale di Geofisica e Vulcanologia, Rome, Italy.

[28]Dipartimento di Scienze della Terra e Geoambientali, University of Bari, Bari, Italy.

[29]IDPA-CNR, Milan, Italy.

[30]Center for Climate Physics, Institute for Basic Science, Busan, South Korea

[31]Pusan National University, Busan, South Korea

[32]Dipartimento di Scienze della Vita, Laboratorio di Palinologia e Paleobotanica, Università di Modena e Reggio Emilia, Modena, Italy.

[33]Leibniz Institute for Applied Geophysics (LIAG), Hannover, Germany.

[34]Institute of Loess Plateau, Shanxi University, Taiyuan, China.

*Correspondence to: wagnerb@uni-koeln.de.

† these authors contributed equally to this work.

68 Precipitation is a key factor for socioeconomic development in densely populated and summer
69 dry regions such as the Mediterranean realm. Seasonal and regional changes are critical, but
70 difficult to project accurately. While current climate model simulations indicate a progressive
71 summer drying over the next century, precipitation changes during winter months are less
72 well constrained[1]. Only a few continental proxy records capable of capturing hydroclimate
73 change cover multiple Northern Hemisphere summer insolation maxima[2,3] with different
74 underlying orbital geometries, necessary to validate climate model data on Quaternary time
75 scales. Here we use a 1.36 million year proxy time series from Lake Ohrid, coupled to a long
76 transient climate model hind cast, to show that high winter precipitation anomalies occur
77 during phases with strong seasonal contrast in insolation and high African summer monsoon
78 activity. While this is counter-intuitive at first sight, our data suggest that increased sea-
79 surface temperatures amplify local cyclogenesis while also refuelling North Atlantic low
80 pressure systems entering the Mediterranean during phases characterized by low continental
81 ice volume and high atmospheric CO_2 concentrations. Comparison with modern reanalysis
82 data shows that current drivers of rainfall amount in the Mediterranean share some similarities
83 to those driving the reconstructed precipitation increases. Our extended record covers multiple
84 insolation maxima and therefore is an important benchmark for testing climate-model
85 performance.

86

87

88 Mediterranean climates are characterized by strong seasonal contrasts between dry and warm
89 summers, and wet and mild winters. The amount and temporal extent of precipitation during
90 the winter half-year (October through March) determines the prevailing type of vegetation
91 and water availability for agrarian land-use in the Mediterranean borderlands. In recent
92 decades, reduction of winter precipitation has become a regular phenomenon in this region,

93 with anthropogenic greenhouse gas (GHG) and aerosol forcing identified as potential
94 contributors[4]. Current climate model simulations, using the Representative Concentration
95 Pathway (RCP) 4.5 and 8.5 scenarios, predict a progressive summer drying over the next
96 century[1]. Precipitation changes during the Northern Hemisphere (NH) winter months are less
97 well constrained, with different simulation runs showing trends both towards wetter and drier
98 conditions. The uncertainty in winter precipitation projections limits the extent to which
99 current modelling approaches are useful for decision makers[5,6].

100 Long-term, empirical baseline data are helpful to constrain uncertainties in climate
101 modelling proxy records. Proxy records and modelling experiments suggest that enhanced
102 precipitation in the Mediterranean region is in phase with the northward shift of the
103 intertropical convergence zone (ITCZ) and increase in African monsoon strength during
104 precession minima causingNorthern Hemisphere summer insolation (NHSI) maxima and
105 winter insolation (NHWI) minima[2,7,8,9]. However, most continental records that are capable of
106 capturing hydroclimate change do not cover multiple NHSI maxima with different underlying
107 orbital geometries. In fact, the majority of records are limited to the Holocene[10,11], yet the
108 Early Holocene NHSI maximum was relatively weak compared to most other Quaternary
109 interglacials, due to lower eccentricity. Terrestrial proxy time series covering multiple NHSI
110 maxima from the Mediterranean region are scarce[2,3]. Sediment records from the
111 Mediterranean Sea provide continuity throughout the Plio-Pleistocene and capture cessations
112 of deep-water ventilation associated with the formation of prominent, organic-rich sapropel
113 layers[12,13]. While multiple factors contribute to sapropel formation, increased freshwater
114 input, particularly from the African continent during NHSI-forced monsoon maxima, is
115 considered the most important[14,15]. Hence, the Mediterranean sapropel record is thought to be
116 an excellent indicator of the relative timing of increased African monsoon strength rather than
117 a direct indicator of precipitation in, and runoff from, the entirety of the Mediterranean realm.
118 Reconstructed precipitation increases in the northern Mediterranean borderlands during

sapropel formation have been interpreted to be a product both of intensified summer and winter precipitation[15,16]. Modelling experiments explain increased winter precipitation by stronger wintertime storm tracks[2] or air-sea temperature difference, and locally induced convective precipitation that dominate freshwater budget changes on obliquity time scales[17]. Alternatively, conceptual models based on proxy time series have suggested increases in the frequency and intensity of low-pressure systems evolving in the Mediterranean region, mostly during fall and early winter[7,8,16]. Hence, a well-dated proxy record covering multiple glacial-interglacial cycles and being sensitive to changes in Mediterranean hydroclimate is key to addressing long-standing questions regarding the underlying mechanisms, timing, and amplitude of precipitation variability under different climate boundary conditions (GHG concentration, orbital geometries, continental ice sheet volume and extent).

Here, we assess precipitation variability in a continuous, independently dated 1.36 Myr sedimentary record from Lake Ohrid (Fig. 1, Extended Data Fig. 1). Climate variations at this site represent broader climate variability across the northern Mediterranean borderlands[18]. We compare our sedimentary proxy time series with transient climate simulation data and prominent monsoon records, to provide a mechanistic understanding of precipitation variability and seasonality, as well as phase relationships to orbital forcing.

Lake Ohrid is of tectonic origin and 293 m deep. The lake is hydrologically open and primarily fed by an extensive karst aquifer system, which supplies ions (mainly Ca^{2+} and HCO_3^-) to the lake and filters particulate matter[19]. Scientific drilling in 2013 resulted in a 584-m-long composite sediment succession from the lake centre, comprised of fine-grained hemi-pelagic muds in the upper 447 m[18,20]. Sedimentation is thought to have been uninterrupted, with no evidence of unconformities or erosion surfaces. Independent age control from 16 interspersed tephra layers in combination with magnetostratigraphy (Fig. 1, Extended Data Fig. 2, Extended Data Table 1, Extended Data Table 2) provides a robust chronological

framework. This framework allows us to match changes in orbital parameters with our proxy data to refine the age-depth relationships. The data demonstrate that the Lake Ohrid record spans the last 1.36 Myr (Fig. 1).

Indicators for detrital input (quartz, potassium), catchment vegetation (arboreal pollen excluding pine (AP-P), deciduous oaks), and hydrological variability (total inorganic carbon (TIC), Ca/K, $\delta^{18}O_{calcite}$, $\delta^{13}C_{calcite}$) show clear orbital-scale cyclicity, also characterized by a precessional (~21 ka) component (Fig. 2; Extended Data Figs 3, 4, and 5). During periods of global ice volume minima and NHSI maxima, we observe prominent peaks in the hydrological and vegetation proxy data (Fig. 2). We interpret these peaks in TIC (mainly from endogenic calcite) and Ca/K (a proxy for the concentration of calcite) to result from enhanced activity of, and ion supply from, the karst aquifers combined with higher aquatic productivity due to warmer conditions[19]. Pollen show a simultaneous increase in vegetation cover, particularly deciduous oaks, during early phases of interglacials. Deciduous oaks benefit from a limited length of the summer dry season[21]. Lower $\delta^{13}C_{calcite}$ values during these periods suggest greater soil development, while lower $\delta^{18}O_{calcite}$ (Extended Data Fig. 3) indicate more positive precipitation/evaporation (P/E) balance[18]. Thus, aquatic and terrestrial datasets suggest higher temperatures along with maxima in annual precipitation amount and potential shorter summer aridity during interglacials (Extended Data Fig. 4).

To provide a better understanding of the observed precipitation variability from the Lake Ohrid record in a regional context, we analysed climate data time series derived from a transient 784 kyr simulation using the earth system model LOVECLIM[22,23] (Extended Data Fig. 6) as well as NOAA reanalysis precipitation data of the Lake Ohrid region for the time period 1979–2017. Temperature time series of the 5°x5° Lake Ohrid grid cell simulated by the LOVECLIM earth system model closely resemble records of first-order global ice volume (Extended Data Fig. 3), such as the LR04 benthic oxygen isotope stack[24] (r=–0.8737 or

169 r^2=0.76 based on 1000-year averages of both data sets). The close match to changes in the
170 amount of detrital siliciclastics and tree pollen (AP-P) confirms the sensitivity of the Lake
171 Ohrid record to global-scale climate fluctuations (Fig. 2; Extended Data Figs 3 and 4). The
172 highest amplitudes in precipitation time series occur during phases of reduced ice volume,
173 with prominent peaks during NHSI maxima. The significant positive relationship between
174 simulated precipitation and our precipitation proxy time series (r^2=0.38) and the persistence of
175 the relationship with the orbital parameters (Extended Data Fig. 4) suggest that the local
176 response recorded at Lake Ohrid also captures changes in regional hydroclimate back to 1.36
177 Ma (Fig. 2).

178 Seen both in paleo records and in climate model simulations, the intensification of NH
179 monsoon systems during precession minima and NHSI maxima is a prominent example of
180 orbitally-forced changes in precipitation variability[14,15,25]. Iconic records of monsoon strength,
181 such as the Chinese speleothem[26], eastern Mediterranean sapropel[12,13,26] and planktonic
182 foraminifera oxygen isotope records[14,15,27], show a positive phase relationship with Lake
183 Ohrid hydrological proxy time series (Fig. 2). Strengthening of NH monsoons results from a
184 northward displacement of atmospheric circulation systems, including the position of the
185 Hadley cells and the ITCZ during NH summer. The shift of the Hadley cell amplifies
186 subsidence over, and persistence of, high-pressure systems in the Mediterranean region,
187 leading to warmer and drier summers[17], and higher sea-surface temperatures (SST)[16,28].
188 Reduced NHWI has highest impact on tropical and subtropical latitudes[2] and leads to low
189 latitude cooling and a southward shift of the ITCZ and the NH Hadley and Ferrel cells.
190 Furthermore, this cooling results in a reduced meridional temperature gradient leading to a
191 weakening of the westerlies based on the thermal wind relationship. The observed
192 relationship between the Lake Ohrid precipitation record (Fig. 2, Extended Data Figs 3 and 4)
193 and the monsoon archives suggests increased precipitation during the winter half-year for this
194 region when NHWI is low.

The Lake Ohrid record, in combination with the transient simulation time series and the NOAA reanalysis data, may provide fundamental insights into the mechanisms invoked by orbital forcing on Mediterranean precipitation. The monthly NOAA reanalysis data of the last 39 years show high precipitation anomalies (defined as above two standard deviations) to occur between the months of September and December (Extended Data Fig. 7a,b). The atmospheric pattern associated with these precipitation events exhibits a trough in the Gulf of Genoa region (Extended Data Fig. 7c), pointing to either increased cyclogenesis over or advection of North Atlantic low pressure into the western Mediterranean region.

The annual cycle of simulated Lake Ohrid precipitation in LOVECLIM is in good agreement with the reanalysis data; the model, however, underestimates the annual mean precipitation (Extended Data Fig. 8b). Maxima in our simulated precipitation time series (defined as above two standard deviations) indicate a positive anomaly from September to November (SON) in agreement with the reanalysis data (Fig. 3, Extended Data Fig. 8b). Despite important differences in the geographical expansion of geopotential height anomalies, both the NOAA and LOVECLIM data show pronounced troughs in the central Mediterranean area and an increase of rainfall during winter half-year in our focus region (Fig. 3). Our observations support previous modelling experiments suggesting that weakened atmospheric stratification and reduced hemispheric temperature contrasts[2], in combination with an increased contrast between warm SST and lower continental air temperatures[17], fuel precipitation increase in the Mediterranean. Such a preconditioning is particularly pronounced at the beginning of the fall, when the stronger thermal inertia of the sea relative to the land promotes local cyclogenesis[17,29]. Local cyclogenesis in combination with the southward shift in the NH atmospheric circulation cells during the winter half-year, which also favours a more southerly trajectory for storm tracks across the North Atlantic and into the Mediterranean[2], lead to increased winter rainfall in the Mediterranean mid-latitudes.

Owing to the significant positive correlation between the simulation and our proxy time series (Extended Data Fig. 4), in terms of timing and amplitude, we infer that this mechanism primarily controlled precipitation at Lake Ohrid for the last 1.36 Myr. Indeed, similar to the NH summer monsoon records, we observe a strong influence of NHSI and a reduced winter temperature contrast in the NH throughout the entirety of our multiproxy time series, suggesting persistence of the mechanism during different climate boundary conditions. The positive phase relationship between the Lake Ohrid precipitation proxy time series and sapropel records (Fig. 2) indicates a strong coherence of African summer monsoon strength and widespread Mediterranean winter half-year precipitation. Some peaks in our precipitation proxy time series, which are not represented by sapropel layers (Fig. 2), may indicate lower monsoon strength and reduced runoff from the African continent or that the general setting required for sapropel deposition and preservation was not established in the Mediterranean Sea during these periods[15]. During colder and drier glacial periods[3] with increased global ice volume, lower atmospheric CO_2 concentrations, and stronger mid-latitude westerlies, insolation forcing on precipitation appears suppressed in our record. This is in agreement with the sensitivity simulations conducted to disentangle the individual effects of orbital forcing, NH ice sheets, and CO_2 on Lake Ohrid precipitation (Extended Data Fig. 6).

Precessional forcing on insolation is not only the key driver of the NH monsoons, it also exerts a strong control on precipitation variability in the Mediterranean mid-latitudes during the Quaternary. Lake Ohrid sediment cores record highly resolved and chronologically well-constrained information on precipitation maxima during phases of lower intrahemispheric temperature contrast and peak SST's over the last 1.36 Myr. The apparent equivalence of the past regional key drivers of precipitation extremes to those produced by continued anthropogenic increase of atmospheric GHG concentrations may help to reduce simulation uncertainties and makes these results also relevant to predictions for the future evolution of Mediterranean climate.

246

247 **References:**

248 1. IPCC, 2013: Annex I: Atlas of Global and Regional Climate Projections [van
249 Oldenborgh, G. J., M. Collins, J. Arblaster, J. H. Christensen, J. Marotzke, S. B. Power,
250 M. Rummukainen and T. Zhou (eds.)]. In: Climate Change 2013: The Physical Sci¬ence
251 Basis. Contribution of Working Group I to the Fifth Assessment Report of the
252 Intergovernmental Panel on Climate Change [Stocker, T. F., D. Qin, G.-K. Plattner, M.
253 Tignor, S. K. Allen, J. Boschung, A. Nauels, Y. Xia, V. Bex and P. M. Midgley (eds.)].
254 Cambridge University Press, Cambridge, United Kingdom and New York, NY, USA
255 (2013).

256 2. Kutzbach, J. E., Chen, G., Cheng, H., Edwards, R. & Liu, Z. Potential role of winter
257 rainfall in explaining increased moisture in the Mediterranean and Middle East during
258 periods of maximum orbitally-forced insolation seasonality. *Clim. Dyn.* **42**, 1079−1095
259 (2014). doi:10.1007/s00382-013-1692-1

260 3. Tzedakis, P. C., Hooghiemstra, H. & Pälike H. The last 1.35 million years at Tenaghi
261 Philippon, revised chronostratigraphy and long-term vegetation trends. *Quat. Sci. Rev.*
262 **25,** 3416−3430 (2006). doi:10.1016/j.quascirev.2006.09.002

263 4. Hoerling, M. et al. On the increased frequency of Mediterranean drought. *J. Climate* **25**,
264 2146−2161 (2012). doi:10.1175/JCLI-D-11-00296.1

265 5. Weisheimer, A. & Palmer, T. N. On the reliability of seasonal climate forecasts. *J. Royal*
266 *Soc., Interface* **11**, 20131162 (2014). doi.org/10.1098/rsif.2013.1162

267 6. Totz, S., Tziperman, E., Coumou, D., Pfeiffer, K. & Cohen, J. Winter Precipitation
268 Forecast in the European and Mediterranean Regions Using Cluster Analysis. *Geophys.*
269 *Res. Lett.* **44**, 12,418–12,426 (2017). doi.org/10.1002/2017GL075674

7. Milner, A. M. et al. Enhanced seasonality of precipitation in the Mediterranean during the early part of the Last Interglacial. *Geology* **40**, 919−922 (2012). doi:10.1130/G33204.1

8. Toucanne, S. et al. Tracking rainfall in the northern Mediterranean borderlands during sapropel deposition. *Quat. Sci. Rev.* **129**, 178−195 (2015). doi:10.1016/j.quascirev.2015.10.016

9. Stockhecke, M. et al. Millennial to orbital-scale variations of drought intensity in the Eastern Mediterranean. *Quat. Sci. Rev.* **133**, 77−95 (2016). doi: 10.1016/ j.quascirev.2015.12.016

10. Roberts, N. et al. Stable isotope records of Late Quaternary climate and hydrology from Mediterranean lakes: the ISOMED synthesis. *Quat. Sci. Rev.* **27**, 2426−2441 (2008). doi:10.1016/j.quascirev.2008.09.005

11. Magny, M. et al. North–south palaeohydrological contrasts in the central Mediterranean during the Holocene: tentative synthesis and working hypotheses. *Clim. Past* **9**, 2043−2071 (2013). doi:10.5194/cp-9-2043-2013

12. Emeis K.-C., Camerlenghi A., McKenzie J. A., Rio D.& Sprovieri R., The occurrence and significance of Pleistocene and Upper Pliocene sapropels in the Tyrrhenian Sea. *Mar. Geol.* **100**, 155−182 (1991). doi:10.1016/0025-3227(91)90231-R

13. Kroon, D. al. Oxygen isotope and sapropel stratigraphy in the Eastern Mediterranean during the last 3.2 million years, in *Proceedings of the Ocean Drilling Program. Scientific results***,** A. H. F. Robertson, K.-C. Emeis, C. Richter, A. Camerlenghi. Eds. (College Station, Texas, 1998), vol. 160, pp 181−190 (1998).

14. Rossignol-Strick, M. Mediterranean Quaternary sapropels, an immediate response of the African monsoon to variation of insolation. *Palaeogeogr. Palaeoclimatol. Palaeoecol.* **49**, 237−263 (1985). doi:10.1016/0031-0182(85)90056-2

15. Rohling, E. J., Marino, G. & Grant, K. M. Mediterranean climate and oceanography, and the periodic development of anoxic events (sapropels). *Earth Sci. Rev*. **143**, 62−97 (2015). doi:10.1016/j.earscirev.2015.01.008

16. Tzedakis, P. C. Seven ambiguities in the Mediterranean palaeoenvironmental narrative. *Quat. Sci. Rev*. **26**, 2042−2066 (2007). doi:10.1016/j.quascirev.2007.03.014

17. Bosmans, J. H. C. et al. Precession and obliquity forcing of the freshwater budget over the Mediterranean. *Quat. Sci. Rev.*, **123**, 16−30 (2015). doi:10.1016/j.quascirev.2015.06.008

18. Wagner, B. et al. The environmental and evolutionary history of Lake Ohrid (FYROM/Albania): Interim results from the SCOPSCO deep drilling project. *Biogeosciences* **14**, 2033−2054 (2017). doi:10.5194/bg-14-2033-2017

19. Vogel, H., Wagner, B., Zanchetta, G., Sulpizio, R. & Rosén, P. A paleoclimate record with tephrochronological age control for the last glacial-interglacial cycle from Lake Ohrid, Albania and Macedonia. *J. Paleolimnol.* **44**, 295−310 (2010). doi:10.1007/s10933-009-9404-x

20. Francke, A. et al. Sedimentological processes and environmental variability at Lake Ohrid (Macedonia, Albania) between 637 ka and the present. *Biogeosciences* **13**, 1179−1196 (2016). doi:10.5194/bg-13-1179-2016

21. Forner, A. et al. Extreme droughts affecting Mediterranean tree species' growth and water-use efficiency: the importance of timing. *Tree Physiol.* **38**, 1127−1137 (2018). doi:10.1093/treephys/tpy022

22. Friedrich, T., Timmermann, A., Tigchelaar, M., Timm, O. E. & Ganopolski, A. Nonlinear climate sensitivity and its implications for future greenhouse warming. *Sci. Adv*. **2** (2016), p. e1501923. doi:10.1126/sciadv.1501923

23. Timmermann, A. & Friedrich, T. Late Pleistocene climate drivers of early human migration. *Nature* **538**, 92−95 (2016). doi:10.1038/nature19365

24. Lisiecki, L. E. & Raymo, M. E. A Pliocene-Pleistocene stack of 57 globally distributed benthic $\delta^{18}O$ records. *Paleoceanography* **20**, PA1003 (2005). doi:10.1029/2004PA001071

25. Cheng, H. et al. The Asian monsoon over the past 640,000 years and ice age terminations. *Nature* **534**, 640−646 (2016). doi:10.1038/nature18591

26. Konijnendijk, T. Y. M., Ziegler, M. & Lourens, L. J. Chronological constraints on Pleistocene sapropel depositions from high-resolution geochemical records of ODP Sites 967 and 968. *Newslett. Stratigr.* **47**, 263−282 (2014). doi:10.1127/0078-0421/2014/0047

27. Colleoni, F., Masina, S., Negri, A. & Marzocchi, A. Plio–Pleistocene high–low latitude climate interplay: a Mediterranean point of view. *Earth Planet. Sci. Lett.* **319–320,** 35−44 (2012). doi:10.1016/j.epsl.2011.12.020

28. Martrat, B., Jimenez-Amat, P., Zahn, R. & Grimalt J. O., Similarities and dissimilarities between the last two deglaciations and interglaciations in the North Atlantic region. *Quat. Sci. Rev.* **99**, 122−134 (2014). doi:10.1016/j.quascirev.2014.06.016

29. Trigo, R. M., Osborne, T. J. & Corte-Real, J. M. The North Atlantic Oscillation influence on Europe: climate impacts and associated physical mechanisms. *Clim. Res*. **20**, 9−17 (2002). doi:10.3354/cr020009

30. Laskar, J. et al. A long-term numerical solution for the insolation quantities of the earth. *Astron. Astrophys*. **428**, 261−285 (2004). doi:10.1051/0004-6361:20041335

Acknowledgments: The Hydrobiological Institute in Ohrid (S. Trajanovski and G. Kostoski) and the Hydrometeorological Institute in Tirana (M. Sanxhaku and B. Lushaj) provided logistic support for site surveys and the scientific drilling campaign. Drilling was carried out by Drilling, Observation and Sampling of the Earth's Continental Crust (DOSECC). A. Skinner provided logistic and technical advice prior and during drilling operation. The Scientific Collaboration on Past Speciation Conditions in Lake Ohrid (SCOPSCO) drilling project was funded by the International Continental Scientific Drilling Program (ICDP), the German Ministry of Higher Education and Research, the German Research Foundation, the University of Cologne, the British Geological Survey, the INGV and CNR (both Italy), and the governments of the republics of North Macedonia and Albania. V. Scao collected the V5 tephra, which was $^{40}Ar/^{39}Ar$ dated with funding from LEFE "INTERMED" grant (CNRS-INSU) to S. Nomade.

Author Contributions: B Wagner and H Vogel designed the study and contributed equally. BW initiated and coordinated the SCOPSCO drilling project and drilling campaign. HV conceived major scientific ideas of this study. A Francke (sedimentology, chronology), T Friedrich (LOVECLIM modelling), T Donders (palynology), J Lacey (isotope geochemistry), and L Sadori (palynology) contributed and oversaw key datasets used in the study. They coordinated together with F Cremer-Wagner, M Leng, E Regattieri, T Wilke and G Zanchetta discussion and interpretations of proxy data groups and model results. Specific data were provided by A Bertini (pollen, MIS 19–21, MIS 25–28, MIS 42–43), N Combourieu-Nebout (pollen, MIS 1–4, MIS 8, MIS 14–15), B Giaccio (tephrostratigraphy), S Joannin (pollen, MIS 1–4, MIS 13–16, MIS 30), J Just (paleomagnetic data), K Kouli (pollen, MIS 6–8, MIS 10, MIS 16–19, MIS 28–30, MIS 33), I Kousis (pollen, MIS 11–12, MIS 15), A Koutsodendris (pollen, MIS 11–12, MIS 15), N Leicher (tephrostratigraphy), A Masi (pollen,

MIS 5–6, MIS 20–25, MIS 31–32), A M Mercuri (pollen, MIS 6, MIS 34), S Nomade (tephrochronology), N Nowaczyk (paleomagnetic data), K Panagiotopoulos (pollen, MIS 7–8, MIS 35–43), O Peyron (pollen, MIS 1–4, MIS 13–16, MIS 30), L Sagnotti (paleomagnetic data), G Sinopoli (pollen, MIS 5–6), R Sulpizio (tephrostratigraphy) and P Torri (pollen MIS 6, MIS 34). S Krastel, K Lindhorst, and T Wonik coordinated the seismic survey of Lake Ohrid, the selection of the coring location and the geophysical measurements needed for core correlation. A Grazhdani, M Melles, J Reed, and Z Levkov contributed to the conception of the work. A Cvetkoska, J Holtvoeth, E Jovanvoska, S Tofilovska, and X Zhang provided micropaleontological and organic geochemistry data, which confirmed that the sediment succession from the DEEP site covers the entire history of Lake Ohrid. A Timmermann provided model infrastructure and resources. All authors contributed to the discussion and interpretation of the data and provided comments and suggestions to the manuscript.

Author Information: Reprints and permissions information is available at www.nature.com/reprints. Authors declare no competing interests. Correspondence and requests for materials should be addressed to wagnerb@uni-koeln.de. Data are available in the main text, in the supplementary materials and in the Pangaea database at https://doi.pangaea.de/10.1594/PANGAEA.896848. Data used for LOVECLIM are available at https://climatedata.ibs.re.kr/grav/data/loveclim-784k.

Figure legends:

Fig. 1. Chronology and location of the Lake Ohrid DEEP site record. (a) The age model is based on tephrostratigraphic correlation of 16 tephra layers to their radiometrically dated proximal deposits (red, first-order tie points) **(b)** tuning of total organic carbon (TOC) minima in the DEEP site record vs. inflection points in insolation and winter season length (blue,

second-order tie points), and cross evaluation of two paleomagnetic age reversals (a; dashed lines). The age model was calculated following the methodological approach for the upper 247 meters composite depth (mcd) of the record[20] (see Methods). For the ages and errors of the tephra layers, see Extended Data Table 1. The tuning points (green) include an error of ±2,000 years. **(c)** The insert shows the location of Lake Ohrid and the approximate position of the intertropical convergence zone (ITCZ) in summer and winter.

Fig. 2. Lake Ohrid precipitation indicators and global monsoon records for the last 1.4 million years. **(a)** Eastern Mediterranean (EM) Sapropel ages (green = sapropel, red = red interval/oxidized sapropel, violet = ghost sapropel)[12,13,27]; **(b)** Chinese Speleostack $\delta^{18}O$ [26] in ‰ relative to VPDB; **(c)** Medstack $\delta^{18}O$ planktonic[28] in ‰ relative to VPDB; SST=sea-surface temperature, SSS=sea-surface salinity; **(d)** Lake Ohrid $\delta^{13}C$ endogenic calcite in ‰ relative to VPDB; **(e)** Lake Ohrid deciduous oaks pollen percentage; **(f)** Lake Ohrid total inorganic carbon (TIC) concentrations; **(g)** Northern Hemisphere winter insolation difference between the tropic of cancer and the arctic circle[30]; **(h)** annual mean precipitation amount for the Lake Ohrid grid cell from the LOVECLIM simulation; **(i)** Lake Ohrid arboreal pollen excluding *Pinus* pollen (AP-P) percentages. Tenaghi Philippon arboreal pollen (AP) percentages[3] **(k)** and LR04 benthic $\delta^{18}O$ stack[25] in ‰ relative to VPDB with odd numbers for interglacials **(l)** are shown for comparison. Red and white diamonds indicate the position of radiometrically dated tephra layers, blue and white diamonds the position of reversals of Earth's magnetic field in the Lake Ohrid sediment record.

Fig. 3. Simulated Lake Ohrid precipitation and atmospheric anomaly pattern associated with precipitation maxima. (a) Simulated precipitation (cm yr^{-1}) for the Lake Ohrid grid cell. Data based on 1,000-year averages. Dashed line indicates two standard deviations above the mean. Red shading highlights precipitation values exceeding two standard deviations. See Methods for details on the model simulations. **(b)** Composite anomalies of September-

November (SON), 800 hPa geopotential height (m, shading) and wind (m s^{-1}, vectors) associated with precipitation maxima shown in (a).

Methods:

Lake and lake hydrology

Lake Ohrid (41°02'N, 20°43'E, 693 m a.s.l.; Fig. 1c) is located in the sub-Mediterranean climate zone with average monthly air temperature ranging from +26°C during summer to -1°C during winter. Precipitation in the Lake Ohrid watershed increases from 698 to 1,194 mm yr^{-1} with increasing altitude and occurs primarily during winter months[31]. The lake is ~30 km long, ~15 km wide, and has a maximum water depth of 293 m (Extended Data Fig. 1). Sublacustrine karst springs (55%), direct precipitation, and river inflow (45%) constitute the water input. Due to an oligotrophic state, bottom waters remain partly oxygenated for several years, although the lake is oligomictic and a complete overturn occurs only every few years at present[32].

Sediment cores

Sediment cores from the Lake Ohrid DEEP site were recovered in spring 2013, using the Deep Lake Drilling System (DLDS) of Drilling, Observation and Sampling of the Earth's Continental Crust (DOSECC) and within the framework of the multinational and interdisciplinary Scientific Collaboration on Past Speciation Conditions in Lake Ohrid (SCOPSCO) project that was co-sponsored by the International Continental Scientific Drilling Program (ICDP). The composite sediment record is based on 6 parallel boreholes that reached a terminal depth of 568 m[33]. Sediment recovery from 0 to 456.1 m composite depth (mcd) is 99.8%. Small gaps occur between 204.719 and 204.804 mcd (8.5 cm) and between 447.89 and 448.19 mcd (30 cm)[33]. Mass movement deposits (<3 cm) occur between 117 and 107 mcd, and between 55 and 50 mcd. Subsampling in the upper 447.12 mcd excluded mass movement and tephra deposits.

Scanning-X-ray fluorescence (XRF) analysis

Scanning-XRF analysis was performed at the University of Cologne, Germany, on split core surfaces at 2.5 mm increments and 10 s dwell time using an ITRAX XRF core scanner (Cox Analytics) equipped with an energy dispersive silicon drift detector and a Cr-tube set to 30 kV/30 mA. Raw data were processed and element-specific photon energy peaks were integrated in Q-spec (Cox Analytics).

Elemental analysis

Elemental analysis was performed on 16-cm-spaced samples (2794 samples, ~480 yr) following freeze-drying and homogenization at the University of Cologne. For total carbon (TC) and total inorganic carbon (TIC) measurements, an aliquot of 40 mg of the homogenized sample material was dispersed in 10 ml deionized water. TC was determined at combustion of 900°C and TIC was measured after treatment with 40% H_3PO_4 at 160°C using a DIMATOC 100 and a DIMATOC 200 (DIMATEC Corp., Germany). The total organic carbon (TOC) content was calculated as the difference between TC and TIC.

Fourier Transform Infrared Spectroscopy (FTIRS)

Relative concentration changes for quartz were assessed using FTIRS, on samples spaced at 32 cm (1462 samples, ~1,000 yr). Measurements were performed using a Bruker Vertex 70 equipped with a lN_2-cooled MCT (mercury-cadmium-telluride) detector, a KBr beam splitter, and a HTS-XT accessory unit (multisampler) in an air-conditioned laboratory at the University of Bern, Switzerland. For this purpose, 11 mg of each sample and 500 mg of oven-dried spectroscopic grade KBr (Uvasol®, Merck Corp.) were homogenized and scanned 64 times at a resolution of 4 cm^{-1} (reciprocal centimetres) for the wavenumber range from 3,750 to 520 cm^{-1} in diffuse reflectance mode. Data processing encompassed a linear baseline correction to remove baseline shifts and tilts by setting two points of the recorded spectrum to zero (3,750 and 2,210–2,200 cm^{-1}). Peak areas diagnostic for symmetric stretching of SiO_4 in

quartz (778 and 798 cm^{-1}), and representative for relative abundance[34,35] were integrated using the OPUS (Bruker Corp.) software package.

Palynology processing and analysis

Pollen analysis was carried out on sediment samples spaced at 64 cm (697 samples, ~2000 yr) following processing, identification, and counting approaches as described in[36]. Dry sediment (1.0–1.5 g) samples were treated with cold HCl (37%vol), cold HF (40%vol), and hot NaOH (10%vol) to dissolve carbonates, silicates, and humic acids, respectively. Glycerin-mounted residues were analysed by transmitted light microscopy to a mean of ~533 (incl. *Pinus*) and ~250 (excl. *Pinus*) grains/sample. Relative abundances are based on the total terrestrial pollen sum excl. *Pinus* due to overrepresentation and potential long-distance transport of this taxon[36]. Deciduous oak abundances represent the combined percentages of *Quercus robur* and *Q. cerris* types[37], which is commonly used as an indicator for mid-elevation, relatively humid forest across the Mediterranean[38,39,40,41].

Isotope analysis

Oxygen and carbon isotopes were analysed on bulk carbonate (calcite)[42] in samples spaced at 16 cm through zones of higher TIC (>0.5%), comprising a total of 1309 sediment samples. The samples were immersed in 5% NaClO solution for 24 h to gently disaggregate the sediment and oxidize reactive organic material. Potential biogenic carbonate was removed by sieving and the <64 μm fraction washed with deionized water, dried at 40°C, and then ground to a fine powder in an agate mortar. CO_2 was evolved from 10 mg $CaCO_3$ powders by reaction with anhydrous H_3PO_4 overnight inside a vacuum at a constant temperature of 25°C. The liberated CO_2 was cryogenically purified under vacuum and collected for analysis on a VG Optima dual inlet mass spectrometer. Oxygen and carbon isotope values are reported in standard delta notation ($\delta^{18}O_{calcite}$ and $\delta^{13}C_{calcite}$, respectively) in per mille (‰) calculated to

the Vienna Pee Dee Belemnite (VPDB) scale using a within-run laboratory standard (MCS) calibrated against international NBS standards. Analytical reproducibility for the within-run standard was <0.1‰ (±1σ) for $\delta^{18}O$ and $\delta^{13}C$.

Magnetostratigraphic analyses

Remanent magnetization in its natural state (NRM) and after step-wise alternating field demagnetization (10 steps up to 100 mT) was measured on ~900 discrete cube (6.3 cm^3) samples with an average 48-cm-spacing at the Paleomagnetic Laboratory at the GeoForschungsZentrum, Potsdam, Germany, using a 2G Enterprises cryogenic magnetometer. Paleomagnetic directions (declination and inclination) were calculated using principle component analysis (PCA) after removal of low-coercivity magnetic overprints. After identification of geomagnetic polarity transitions, ~500 additional samples were taken at 2 to 3-cm-spacing across these transitions for high-resolution analysis at the Istituto Nazionale di Geofisica e Vulcanologia, Rome, Italy, using the same analytical set up and routine as in Potsdam. As glacial intervals of the core contain diagenetically formed greigite, which overprints the primary paleomagnetic signal[43], paleomagnetic transitions are faithfully preserved only in interglacial intervals, at the base of the Jaramillo sub-Chron (373.8 mcd) and at the Matuyama/Brunhes (M/B) boundary (287.6 mcd).

Tephrostratigraphic analysis

Eleven tephra and three cryptotephra layers have successfully been identified in the upper 247 mcd of the record[44,45,46]. Two additional tephra layers from the lower (>247 mcd) part of the DEEP site record are introduced here. The tephrostratigraphic correlation of these tephras is based on geochemical fingerprinting of single glass shards using Wavelength Dispersive Electron Microprobe Analysis (WDS-EPMA) as described in [44].

$^{40}Ar/^{39}Ar$ dating was performed at the LSCE facility (CEA, UVSQ and University Paris-Saclay). V5 tephra (=OH-DP-2669 layer) was collected in Montalbano-Jonico (Southern Italy, N40°17'32.8''; E16°33'27.4''). Twenty pristine sanidine crystals, of the fraction 0.6-1.0 mm, were extracted from V5 and irradiated for 2 h in the Cd-lined, in-core CLICIT facility of the Oregon State University TRIGA reactor (Irradiation CO 001). Subsequently, 14 crystals were individually loaded in a copper sample holder and put into a double vacuum Cleartran window. Each crystal was individually fused using a Synrad CO_2 laser at 10-15% of nominal power (~50 W). The extracted gas was purified for 10 min by two hot GP 110 and two GP 10 getters (ZrAl). Ar isotopes (^{36}Ar, ^{37}Ar, ^{38}Ar, ^{39}Ar and ^{40}Ar) were analysed by mass spectrometry using a VG5400 equipped with an electron multiplier Balzers 217 SEV SEN coupled to an ion counter. Neutron fluence J for each sample is calculated using co-irradiated Alder Creek Sanidine (ACs-2) standard with an age of 1.1891Ma [47] and the total decay constant of [48]. J-values computed from standard grains is 0.00053220 ± 0.00000160. Mass discrimination was estimated by analysis of air pipette throughout the analytical period, and was relative to a $^{40}Ar/^{36}Ar$ ratio of 298.56 [49].

Tephra OH-DP-2669 is a 2.5 cm thick, yellowish layer with sharp upper and lower boundaries comprising up to 500 µm large platy glass shards and minor elongated micropumices. Its distinct trachytic composition (Extended Data Fig. 2) and the stratigraphic position between the M/B boundary (287.6 mcd) and OH-DP-2060 (Tufo di Bagni Albula, 524.84 ka [44]; Extended Data Table1) narrow potential tephrostratigraphic equivalents. Tephra layer SC1-35.30/SUL2-1 from the Sulmona basin in the Italian Apennines is the only tephra with a similar trachytic composition[50,51] for this interval (Extended Data Fig. 2, Extended Data Table 2). SC1-35.30/SUL2-1 was correlated with tephra V5 from the MJS [52,53]. The majority of the SC1-35.30/SUL2-1 and OH-DP-2669 analyses correlate well with the more evolved group of V5 (V5b: SiO_2 >63% wt.; CaO <1.5% wt.). Only few analyses plot in the field of the less evolved group V5a (Extended Data Fig. 2, Extended Data Table 2). Tephra

552 layer SUL2-1 and V5 were $^{40}Ar/^{39}Ar$ dated at 722.8±2.4 ka[50] and 719.5±12.6 ka[53],
553 respectively.
554 The previous proposed correlation of SUL2-1/V5 with the Parmenide ash found in the
555 Crotone basin[50,52] is not considered here due to a slightly younger $^{40}Ar/^{39}Ar$ age of the
556 Parmenide ash (710±5 ka) [54,55,56] and the differences in the geochemical data to OH-DP-2669
557 (Extended Data Fig. 2, Extended Data Table 2).
558 Tephra OH-DP-2898 is a ~0.8 cm thick, whitish-yellowish band of lenses comprising
559 fine-grained glass shards with a high degree of vesicularity and a phonolitic composition
560 (Extended Data Fig. 2). It is located ~2 m below the M/B boundary, in calcareous sediments
561 indicative for interglacial conditions[20]. The comparison of OH-DP-2898 glass composition
562 with those of Sulmona tephra SUL2-19, -20, -25, -29 and -31 in a similar
563 magnetostratigraphic position exclude a correlation (Extended Data Fig. 2). Other Sulmona
564 tephra close to the M7B transition, SUL2-22, -23, and -27, have a composition similar to OH-
565 DP-2898, but SUL2-23 has slightly lower alkali and higher CaO, FeO, TiO_2 concentrations
566 (Extended Data Fig. 2, Extended Data Table 2). SUL2-27 is geochemically indistinguishable
567 from OH-DP-2898, but deposited in glacial sediments of the MIS 20 [57]. SUL2-22 is also
568 geochemically indistinguishable from OH-DP-2898 and shares a similar stratigraphic position
569 below the M/B boundary[58,59] and at the transition from MIS 20 to MIS 19 [57]. A correlation of
570 OH-DP-2898 with tephra V4 from the MJS is not possible due to differences in the
571 compositional range (Extended Data Fig. 2, Extended Data Table 2) and a younger $^{40}Ar/^{39}Ar$
572 age of 773.9±1.3 ka of V4 [52], quasi-synchronous position during the ^{10}Be peak or M/B
573 transition[60]. Also a correlation of OH-DP-2898/SUL2-22 with tephra V3 of the MJS
574 (801.2±19.5 ka) is excluded due to differences in the geochemical composition (Extended
575 Data Fig. 2, Extended Data Table 2) and deposition of V3 during glacial conditions of MIS 20
576 [60]. The Pitagora ash from the Crotone basin is found in a similar magneto- and
577 climatostratigraphic position [55,61,62], but differs geochemically from OH-DP-2898/SUL2-22.

Therefore, we regard a correlation of OH-DP-2898 with SUL2-22 as most robustly and use its $^{40}Ar/^{39}Ar$ age of 791.9±1.9 ka [58] for our chronology.

In addition to the new tephra correlations, we updated ages for the upper tephra layers (Extended Data Table 1). This update includes the Campanian Ignimbrite (Y-5/OH-DP-0169)[63] and tephra layers OH-DP-0404/POP2 and OH-DP-0435/X-6, based on new results from the Sulmona section[64]. The tephrostratigraphy of the Fucino record[65] improved and reassessed the correlations established for OH-DP-0617 and OH-DP-0624 [44]. $^{40}Ar/^{39}Ar$ dating of TF-17, correlated to OH-DP-0624, yielded a much more precise age of 158.8 ± 3.0 ka, which replaced the age of Vico B/OH-DP-0617 (162±6 ka)[66].

Furthermore, the correlation of cryptotephra OH-DP-1700.6 with the Vico β eruption[45] provided a new chronological tie-point at 410±2 ka [67]. The previously established correlation of tephra layer OH-DP-1955 with tephra layer SC-5 from the Mercure basin[44] was rejected in the light of its large uncertainty (±10.9 ka) and the new tephrostratigraphic data.

Reassessment of the raw Ar-isotope data of SC1-35.30/SUL2-1, the equivalent to OH-DP-2669, by updating the value of the atmospheric Ar-composition ($^{40}Ar/^{36}Ar$: 298.5 instead of 295.5 originally) and removing xenocrysts[58] yielded a new age of 715.02±5.4 ka (Extended Data Table 1) using the decay constant of [48] and an age of 1.1891 Ma for the ACs-2 flux standard[47]. Our new $^{40}Ar/^{39}Ar$ age of V5 (716.2±5.4 ka; MSWD = 0.8, P = 0.7) is undistinguishable within uncertainty and thus used for our chronology. All other $^{40}Ar/^{39}Ar$ used were recalculated using the software ArAR[68] with a given decay constant and age for ACs-2 (1.1891 Ma) and Fish Canyon sanidines (FCs) ages of 28.294 Ma.

Chronology

Following the methodological approach for the upper 247 mcd of the record[20], the chronology of the DEEP site sediment succession down to 447.12 mcd uses tephrochronological data[44,45,46] as 1st-order tie points and tuning of climate-sensitive proxy data (TOC; ~480 yr resolution)

against orbital parameters as 2nd-order tie points considering that maxima in TIC represent interglacial periods[19,20]. Some chronologically well-constrained tephra layers deposited at the DEEP site since the penultimate glacial period (Y-5, X-6, P-11, and A11/12) occur at depths where TOC shows minima at times of the perihelion passage in March[20]. These perihelion passages in March correspond to the inflection points of increasing local summer insolation (21st June) and winter-season length (number of days between the September and March equinoxes) at the latitude of Lake Ohrid (41°N; Fig. 1). Increasing summer insolation promotes high summer temperatures, primary productivity in the water column and increases organic matter (OM) supply to the sediments. An extended winter season improves lake-water mixing which enhances oxidation of OM in the water column and the surface sediments[20]. Thus, minima in TOC result from moderate OM supply to the sediments and improved oxidation of OM at the sediment surface and are due to their available high temporal resolution in the DEEP site record used for tuning purposes.

The independent chronological information obtained from the 16 tephra and cryptotephra layers and 66 2nd-order tie points obtained from orbital tuning were cross evaluated by the two paleomagnetic age constraints (base of the Jaramillo sub-Chron and Matuyama/Brunhes M/B; Fig. 1). The age model was calculated using Bacon 2.2 [69], considering overall uniform (mem.strength=60, mem.mean=0.9, thick=80 cm) sedimentation rates (acc.shape=1.5, acc. mean=20) at the DEEP site[33]. An error of ±2,000 years was applied to the 2nd-order tie points to account for tuning inaccuracy. The 95% confidence intervals of ages for specific depths produced by the Bacon Bayesian age modelling average at ±5,500 years with a maximum of ±10,680 years. The resulting chronology implies that the upper 447.12 m of the DEEP site record covers the last 1.364 Myr, continuously.

We[20] evaluated the DEEP site's chronology against the 0-160 ka U/Th dated Soreq Cave speleothem record[70] and found agreement within errors of the chronologies. Arboreal

pollen (AP) percentages in the DEEP site record are also in agreement with those from the orbitally-tuned Tenaghi Philippon record[3] back to 1.364 Ma (Fig. 2).

Model simulations and forcing

Transient simulations with the Earth system model LOVECLIM were conducted to study the impacts of orbital forcing, Northern Hemisphere (NH) ice sheets, and variations in atmospheric greenhouse gases (GHGs) on glacial-interglacial climate change.

LOVECLIM is a coupled ocean-atmosphere-sea ice-vegetation model[71]. The atmospheric component of LOVECLIM is the spectral T21, three-level model ECBilt[72] based on quasi-geostrophic equations extended by estimates of ageostrophic terms. The ocean-sea ice component of LOVECLIM consists of a free-surface Ocean General Circulation Model with a 3°x3° horizontal resolution coupled to a dynamic-thermodynamic sea-ice model[73]. Atmosphere and ocean components are coupled through the exchange of freshwater and heat fluxes. The vegetation model VECODE[74] computes the evolution of terrestrial vegetation cover based on annual mean surface temperature and precipitation.

The transient simulations of the last 784,000 years were forced by time-dependent boundary conditions for orbital parameters, atmospheric GHG concentrations, NH ice sheet orography, and albedo following the methodology described in[75]. The orbital forcing was calculated according to[76]. Atmospheric GHG concentrations were prescribed according to reconstructions from EPICA Dome C for CO_2[77] as well as CH_4 and N_2O[78]. Orbital forcing and atmospheric GHG concentrations were updated every model year. The effects of NH ice sheets on albedo and land topography were prescribed according to[79]. The forcing was applied with an acceleration factor of 5, which compresses 784,000 forcing years into 156,000 model years. This acceleration factor is appropriate for quickly equilibrating surface variables. The model simulation is an updated version of the one presented in[75] and uses a higher climate

654 sensitivity resulting in a better representation of the glacial-interglacial surface temperature
655 amplitude[23].
656 Four sensitivity simulations were conducted in addition to the full-forcing simulation
657 described above (Extended Data Fig. 6). The sensitivity simulations cover the last four glacial
658 cycles (408,000 years) and aim at exploring the individual effects of atmospheric GHGs, NH
659 ice sheets and orbital parameters to glacial-interglacial climate change. The first sensitivity
660 simulation uses transient forcing as described above but constant preindustrial (PI)
661 atmospheric GHG concentrations. The "GHG effect" can then be calculated as the difference
662 between the simulation using the full forcing and this simulation. The second sensitivity
663 simulation uses transient forcing as described above but constant PI NH ice sheets (extent and
664 albedo). The "NH ice sheet effect" is calculated as the difference between the full-forcing
665 simulation and this simulation. Two simulations were designed to study the role of orbital
666 forcing under warm and cold climate. For both simulations, transient orbital parameters are
667 used. However, one simulation was run under constant PI atmospheric CO_2 concentration of
668 280 ppm, whereas the second simulation uses a constant atmospheric CO_2 concentration of
669 200 ppm resulting in a colder background climate.
670
671 **Data analysis**
672 To assess the temporal evolution of dominant periodicities in the DEEP site TIC and
673 deciduous oak pollen percentage data, a wavelet power spectrum was computed for the
674 respective time series. The time series were resampled at regular intervals (linear
675 interpolation) at 0.3 kyr (TIC) and 1.0 kyr (pollen), and subsequently submitted to continuous
676 wavelet transform (CWT, Morlet window) using PAST v.3.21 software[80] following the
677 approach by [81]. Results of the CWT show persistent presence of 100 kyr and ~21 kyr orbital
678 frequencies, and a clear presence of 41 kyr in the early half of the pollen record. Relative to

679 the pollen, the CWT results of the TIC show a more pronounced 100 kyr cyclicity over the
680 entire record, and less pronounced 21 kyr signals.
681 To quantitatively test the observed correlation between deciduous oak and TIC
682 maxima against precession forcing, the bandpass-filtered 18–25 kyr component of the proxy
683 data was regressed against precession based on the La2004 orbital solution[30].
684 Partial least squares regression (PLSR) was used to test the correlation of TIC and
685 deciduous oaks as predictive variables with LOVECLIM temperature and precipitation output
686 data. PLSR was performed using SIMCA 14 (Sartorius Stedim Biotech). All datasets were
687 filtered using a frequency centred at 0.05 and a bandwidth of 0.02 prior to multivariate
688 statistical analysis to accommodate for slight age offsets between proxy and simulation data.
689

690 **Methods and Extended Data files references:**

691 31. Popovska, C. & Bonacci, O. Basic data on the hydrology of Lakes Ohrid and Prespa.
692 *Hydrol. Process*. **21**, 658–664 (2007). doi:10.1002/hyp.6252

693 32. Matzinger, A., Spirkovski, Z., Patceva, S. & Wüest A. Sensitivity of ancient Lake Ohrid
694 to local anthropogenic impacts and global warming, *J. Great Lakes Res*. **32**, 158–179
695 (2006). doi:10.3394/0380-1330(2006)32[158:SOALOT]2.0.CO;2

696 33. Wagner, B. et al. The SCOPSCO drilling project recovers more than 1.2 million years of
697 history from Lake Ohrid. *Sci. Drill*. **17**, 19−29 (2014). doi:10.5194/sd-17-19-2014

698 34. Farmer, V. C. The infrared spectra of minerals, edited by: V. C. Farmer, Mineralogical
699 Society Monograph 4, 227 pp, Adlard & Son, Dorking, Surrey, (1974).

700 35. Chukanov, N. V. *Infrared Spectra of Mineral Species*. Springer, Dordrecht, Heidelberg,
701 New York, London (2014). doi:10.1007/978-94-007-7128-4

36. Sadori, L. et al. Pollen-based paleoenvironmental and paleoclimatic change at Lake Ohrid (south-eastern Europe) during the past 500 ka. *Biogeosciences* **13**, 1423–1437 (2016). doi:10.5194/bg-13-1423-2016

37. Beug, H.-J. *Leitfaden der Pollenbestimmung für Mitteleuropa und angrenzende Gebiete*. Verlag Dr. Friedrich Pfeil, München, Germany (2004).

38. Cheddadi, R. et al. Imprints of glacial refugia in the modern genetic diversity of *Pinus sylvestris*. *Global Ecol. Biogeogr*. **15**, 271–282 (2006). doi:10.1111/j.1466-8238.2006.00226.x

39. Rossignol-Strick, M. The Holocene climatic optimum and pollen records of sapropel 1 in the Eastern Mediterranean, 9000–6000 BP. *Quat. Sci Rev*. **18**, 515–530 (1999). doi:10.1016/S0277-3791(98)00093-6

40. Langgut, D., Almogi-Labin, A., Bar-Matthews, M. & Weinstein-Evron, M. Vegetation and climate changes in the South Eastern Mediterranean during the Last Glacial–Interglacial cycle (86 ka): new marine pollen record. *Quat. Sci Rev*. **30**, 3960–3972 (2011). doi:10.1016/j.quascirev.2011.10.016

41. Combourieu-Nebout, N. et al. Climate changes in the central Mediterranean and Italian vegetation dynamics since the Pliocene. *Rev. Palaeobot. Palynol*. **218**, 127–147 (2015). doi:10.1016/j.revpalbo.2015.03.001

42. Lacey, J. H. et al. Northern Mediterranean climate since the Middle Pleistocene: a 637 ka stable isotope record from Lake Ohrid (Albania/Macedonia). *Biogeosciences* **13**, 1801−1820 (2016). doi:10.5194/bg-13-1801-2016

43. Just, J. et al. Environmental control on the occurrence of high-coercivity magnetic minerals and formation of iron sulfides in a 640 ka sediment sequence from Lake Ohrid (Balkans). *Biogeosciences* **13**, 2093–2109 (2016). doi:10.5194/bg-13-2093-2016

44. Leicher, N. et al. First tephrostratigraphic results of the DEEP site record from Lake Ohrid (Macedonia and Albania). *Biogeosciences* **13**, 2151–2178 (2016). doi:10.5194/bg-13-2151-2016

45. Kousis, I. et al. Centennial-scale vegetation dynamics and climate variability in SE Europe during Marine Isotope Stage 11 based on a pollen record from Lake Ohrid. *Quat. Sci. Rev*. **190**, 20−38 (2018). doi:10.1016/j.quascirev.2018.04.014

46. Francke, A. et al. Sediment residence time reveals Holocene shift from climatic to vegetation control on catchment erosion in the Balkans. *Global Planet. Change* **177**, 186–200. 2019. doi:10.1016/j.gloplacha.2019.04.005

47. Niespolo, E. M., Rutte, D., Deino, A. L. & Renne, P. R. Intercalibration and age of the Alder Creek sanidine $^{40}Ar/^{39}Ar$ standard. *Quat. Geochronol*. **39**, 205−213 (2017). doi:10.1016/j.quageo.2016.09.004

48. Renne, P. R., Balco, G., Ludwig, K. R., Mundil, R. & Min, K. Response to the comment by W. H. Schwarz et al. on "Joint determination of ^{40}K decay constants and $^{40}Ar*/^{40}K$ for the Fish Canyon sanidine standard, and improved accuracy for $^{40}Ar/^{39}Ar$ geochronology" by P. R. Renne et al. (2010). *Geochim. Cosmochim. Acta* **75**, 5097−5100 (2011). doi:10.1016/j.gca.2010.06.017

49. Lee, J. Y. et al. A redetermination of the isotopic abundances of atmospheric Ar. *Geochim. Cosmochim. Acta* **70**, 4507−4512 (2006). doi:10.1016/j.gca.2006.06.1563

50. Giaccio, B. et al. Revised Chronology of the Sulmona Lacustrine Succession, Central Italy. *J. Quat. Sci.* **28**, 545−551 (2013). doi:10.1002/jqs.2647

51. Giaccio, B. et al. Tephra layers from Holocene lake sediments of the Sulmona Basin, Central Italy: implications for volcanic activity in Peninsular Italy and tephrostratigraphy

749 in the Central Mediterranean area. *Quat. Sci. Rev*. **28**, 2710−2733 (2009).
750 doi:10.1016/j.quascirev.2009.06.009

751 52. Petrosino, P. et al. The Montalbano Jonico marine succession: An archive for distal
752 tephra layers at the Early–Middle Pleistocene boundary in southern Italy. *Quat. Internat*.
753 **383**, 89−103 (2015). doi:10.1016/j.quaint.2014.10.049

754 53. Ciaranfi, N. et al. Integrated stratigraphy and astronomical tuning of Lower–Middle
755 Pleistocene Montalbano Jonico section (Southern Italy). *Quat. Internat.* **219**, 109−120
756 (2010). doi:10.1016/j.quaint.2009.10.027

757 54. Massari, F. et al. Interplay between tectonics and glacio-eustasy: Pleistocene succession
758 of the Crotone basin, Calabria (southern Italy). *Geol. Soc. Am. Bull*. **114**, 1183−1209
759 (2002). doi:10.1130/0016-7606(2002)114<1183:IBTAGE>2.0.CO;2

760 55. Capraro, L. et al. Climatic patterns revealed by pollen and oxygen isotope records across
761 the Matuyama-Brunhes Boundary in the central Mediterranean (southern Italy). *Geol.*
762 *Soc., London, Spec. Publ*. **247**, 159−182 (2005). doi:10.1144/GSL.SP.2005.247.01.09

763 56. Capraro, L. et al. Chronology of the Lower–Middle Pleistocene succession of the south-
764 western part of the Crotone Basin (Calabria, Southern Italy). *Quat. Sci. Rev*. **30**,
765 1185−1200 (2011). doi:10.1016/j.quascirev.2011.02.008

766 57. Giaccio, B. et al. Duration and dynamics of the best orbital analogue to the present
767 interglacial. *Geology* **43**, 603−606 (2015). doi:10.1130/G36677.1

768 58. Sagnotti, L. et al. Extremely rapid directional change during Matuyama-Brunhes
769 geomagnetic polarity reversal. *Geophys. J. Internat*. **199**, 1110−1124 (2014).
770 doi:10.1093/gji/ggu287

59. Sagnotti, L. et al. How fast was the Matuyama–Brunhes geomagnetic reversal? A new subcentennial record from the Sulmona Basin, central Italy. *Geophys. J. Internat*. **204**, 798−812 (2016). doi:10.1093/gji/ggv486

60. Simon, Q. et al. Authigenic $^{10}Be/^{9}Be$ ratio signature of the Matuyama–Brunhes boundary in the Montalbano Jonico marine succession. *Earth Planet. Sci. Lett.* **460**, 255−267 (2017). doi:10.1016/j.epsl.2016.11.052

61. Rio, D. et al. Reading Pleistocene eustasy in a tectonically active siliciclastic shelf setting (Crotone peninsula, southern Italy). *Geology* **24**, 743−746 (1996). doi:10.1130/0091-7613(1996)024<0743:RPEIAT>2.3.CO;2

62. Macri, P., Capraro, L., Ferretti, P. & Scarponi, D. A high-resolution record of the Matuyama-Brunhes transition from the Mediterranean region: The Valle di Manche section (Calabria, Southern Italy). *Phys. Earth Planet. Inter.* **278**, 1−15 (2018). doi:10.1016/j.pepi.2018.02.005

63. Giaccio, B., Hajdas, I., Isaia, R., Deino, A. & Nomade, S. High-precision ^{14}C and $^{40}Ar/^{39}Ar$ dating of the Campanian Ignimbrite (Y-5) reconciles the time-scales of climatic-cultural processes at 40 ka. *Sci. Rep.* **7**, 45940 (2017). doi:10.1038/srep45940

64. Regattieri, E., et al. A last Interglacial record of environmental changes from the Sulmona Basin (central Italy). *Palaeogeogr. Palaeoclimatol. Palaeoecol*. **472**, 51−66 (2017). doi:10.1016/j.palaeo.2017.02.013

65. Giaccio, B. et al. First integrated tephrochronological record for the last ~190 kyr from the Fucino Quaternary lacustrine succession, central Italy. *Quat. Sci. Rev.* **158**, 211−234 (2017). doi:10.1016/j.quascirev.2017.01.004

66. Laurenzi, M. A. & Villa, I. $^{40}Ar/^{39}Ar$ chronostratigraphy of Vico ignimbrites. *Period. Mineral.* **56**, 285−293 (1987)

795 67. Karner, D. B., Marra, F. & Renne, P. R. The history of the Monti Sabatini and Alban
796 Hills volcanoes: groundwork for assessing volcanic-tectonic hazards for Rome. *J.*
797 *Volcanol. Geotherm. Res.* **107**, 185−219 (2001). doi: 10.1016/S0377-0273(00)00258-4

798 68. Mercer, C. M. & Hodges, K.V. ArAR — A software tool to promote the robust
799 comparison of K–Ar and $^{40}Ar/^{39}Ar$ dates published using different decay, isotopic, and
800 monitor-age parameters. *Chem. Geol*. **440**, 148−163 (2016).
801 doi:10.1016/j.chemgeo.2016.06.020

802 69. Blaauw, M. & Christen, J. A. Flexible paleoclimate age-depth models using an
803 autoregressive gamma process. *Bayes. Analys*. **6**, 457−474 (2011).
804 doi:10.1214/ba/1339616472

805 70. Grant, K. M. et al. Rapid coupling between ice volume and polar temperature over the
806 past 150,000 years. *Nature* **491**, 744–747 (2012). doi:10.1038/nature11593

807 71. Goosse, H. et al. Description of the Earth system model of intermediate complexity
808 LOVECLIM version 1.2. *Geosci. Model Dev*. **3**, 603–633 (2010). doi:10.5194/gmd-3-
809 603-2010

810 72. Opsteegh, J. D., Haarsma, R. J., Selten, F. M. & Kattenberg A. ECBILT: a dynamic
811 alternative to mixed boundary conditions in ocean models. *Tellus, Ser. A, Dyn. Meterol.*
812 *Oceanogr*. **50,** 348–367 (1998). doi:10.3402/tellusa.v50i3.14524

813 73. Goosse, H. & Fichefet, T. Importance of ice-ocean interactions for the global ocean
814 circulation: A model study. *J. Geophys. Res*. **104**, 23337–23355 (1999).
815 doi:10.1029/1999JC900215

816 74. Brovkin, V., Ganopolski, A. & Svirezhev, Y. A continuous climate-vegetation
817 classification for use in climate-biosphere studies. *Ecol. Modell.* **101,** 251–261 (1997).
818 doi:10.1016/S0304-3800(97)00049-5

819 75. Timmermann, A. et al. obliquity and CO_2 effects on Southern Hemisphere climate during
820 the past 408 ka. *J. Clim.* **27**, 1863–1875 (2014). doi:10.1175/JCLI-D-13-00311.1

821 76. Berger, A. Long-term variations of daily insolation and Quaternary climate change. *J.*
822 *Atmos. Sci*. **35**, 2362–2367 (1978). doi:10.1175/1520-
823 0469(1978)035<2362:LTVODI>2.0.CO;2

824 77. Lüthi, D. et al. High-resolution carbon dioxide concentration record 650,000-800,000
825 years before present. *Nature* **453**, 379–382 (2008). doi:10.1038/nature06949

826 78. EPICA community members. Eight glacial cycles from an Antarctic ice core. *Nature* **429**,
827 623–628 (2004). doi:10.1038/nature02599

828 79. Ganopolski, A. & Calov, R. The role of orbital forcing, carbon dioxide and regolith in
829 100 kyr glacial cycles. *Clim. Past*, **7**, 1415–1425 (2011). doi: 10.5194/cp-7-1415-2011

830 80. Hammer, O. PAleontological Statistics (PAST) Version 3.21 reference manual, Natural
831 History Museum, University of Oslo (2018). https://folk.uio.no/ohammer/past/

832 81. Torrence, C. & Compo, G. P. A practical guide to wavelet analysis. *Bull. Am. Meteorol.*
833 *Soc.* **79**, 61−78. (1998). doi:10.1175/1520-0477(1998)079<0061:APGTWA>2.0.CO;2

834 82. Lindhorst, K. et al. Sedimentary and tectonic evolution of Lake Ohrid
835 (Macedonia/Albania). *Basin Res*. **27**, 84−101 (2015). doi:10.1111/bre.12063

836 83. Melard, G. Algorithm AS 197: A fast algorithm for the exact likelihood of
837 autoregressive-moving average models. *Appl. Stat.* **33**,104–114 (1984).
838 doi:10.2307/2347672

839 84. Bar-Matthews, M., Ayalon, A., Gilmour, M., Matthews, A. & Hawkesworth, C. J. Sea-
840 land oxygen isotopic relationships from planktonic foraminifera and speleothems in the
841 Eastern Mediterranean region and their implication for paleorainfall during interglacial

intervals. *Geochim. Cosmochim. Acta* **67**, 3181−3199 (2003). doi: 10.1016/S0016-7037(02)01031-1

85. Zanchetta, G. et al. Aligning and synchronization of MIS5 proxy records from Lake Ohrid (FYROM) with independently dated Mediterranean archives: implications for DEEP core chronology. *Biogeosciences*, **13**, 2757–2768 (2016). doi:10.5194/bg-13-2757-2016

86. Le Bas, M. J. Le Maitre, R. W. Streckeisen, A. & Zanettin, B. A Chemical Classification of Volcanic Rocks Based on the Total Alkali-Silica Diagram. *J. Petrol*. **27**, 745–750, (1986). doi:10.1093/petrology/27.3.745

87. Wagner, B. et al. The last 40 ka tephrostratigraphic record of Lake Ohrid, Albania and Macedonia: a very distal archive for ash dispersal from Italian volcanoes. *J. Volcanol. Geotherm. Res.* **177**, 71–80 (2008). doi:10.1016/j.jvolgeores.2007.08.018.

88. Zanchetta, G. et al. Tephrostratigraphy, chronology and climatic events of the Mediterranean basin during the Holocene: An overview. *Holocene* **21**, 33–52 (2011). doi:10.1177/0959683610377531

89. Siani, G., Sulpizio, R., Paterne, M. & Sbrana, A. Tephrostratigraphy study for the last 18,000 C-14 years in a deep-sea sediment sequence for the South Adriatic. *Quat. Sci. Rev*. **23**, 2485–2500 (2004). doi:10.1016/j.quascirev.2004.06.004.

90. Albert, P. G. et al. Revisiting the Y-3 tephrostratigraphic marker: a new diagnostic glass geochemistry, age estimate, and details on its climatostratigraphical context, *Quat. Sci. Rev*. **118**, 105–121 (2015). doi:10.1016/j.quascirev.2014.04.002

91. Satow, C. et al. A new contribution to the Late Quaternary tephrostratigraphy of the Mediterranean: Aegean Sea core LC21, *Quat. Sci. Rev*. **117**, 96–112 (2015). doi:10.1016/j.quascirev.2015.04.005

92. Giaccio, B. et al. Isotopic (Sr-Nd) and major element fingerprinting of distal tephras: an application to the Middle-Late Pleistocene markers from the Colli Albani volcano, central Italy. *Quat. Sci. Rev*. **67**, 190–206 (2013). doi: 10.1016/j.quascirev.2013.01.028

93. Petrosino, P., Jicha, B. R., Mazzeo, F. C. & Russo Ermolli, E. A high resolution tephrochronological record of MIS 14–12 in the Southern Apennines (Acerno Basin, Italy). *J. Volcanol. Geotherm. Res*. **274**, 34–50 (2014). doi:10.1016/j.jvolgeores.2014.01.014

94. Marra, F., Karner, D. B., Freda, C., Gaeta, M. & Renne, P. Large mafic eruptions at Alban Hills Volcanic District (Central Italy): Chronostratigraphy, petrography and eruptive behavior. *J. Volcanol. Geotherm. Res*. **179**, 217–232 (2009). doi:10.1016/j.jvolgeores.2008.11.009

Data Availability

Data are available in the main text, in the supplementary materials and in the Pangaea database at https://doi.pangaea.de/10.1594/PANGAEA.896848. Data used for LOVECLIM are available at https://climatedata.ibs.re.kr/grav/data/loveclim-784k.

Code Availability

Model data produced by the LOVECLIM simulations are available through the data centre of the IBS Center for Climate Physics: https://climatedata.ibs.re.kr/grav/data/loveclim-784k. Additional data are available upon request made to Tobias Friedrich (tobiasf@hawaii.edu).

Extended Data Legends

Extended Data Figure 1 | Map of Lake Ohrid and its surrounding area. Geology, topography, and bathymetry compiled from[19,82] and geological maps of Albania and North Macedonia. The lake is located at an altitude of 693 m a.s.l. and has a maximum water depth of 293 m. The water depth at the DEEP drill site is 240 m.

Extended Data Figure 2 | Correlation of tephra layers at the DEEP site with tephra layers found in mid-distal records. Bi-oxide plots of **(a)** CaO vs. FeO_{total}, **(b)** CaO vs. Al_2O_3, **(c)** CaO vs. TiO_2, **(d)** Na_2O vs. K_2O, and **(e)** total alkali vs. silica (TAS) diagram[86] show the correlation of OH-DP-2669 with the tephra layers SC1-35.30/SUL2-1/V5 and the differences to the Parmenide ash. Bi-oxide plots of **(f)** CaO vs. FeO_{total}, **(g)** CaO vs. Al_2O_3, **(h)** CaO vs. TiO_2, **(i)** Na_2O vs. K_2O, and **(k)** TAS diagram show the correlation of OH-DP-2898 with tephra SUL2-22 and the differences to SUL2-23, -27, -31, V4, V3, and the Pitagora ash. Error bars of the Parmenide Ash refer to [54].Tephra ages, geochemical data, tephrostratigraphic discussion and references are provided in Extended Data Tables 1 and 2 and in Methods.

Extended Data Figure 3 | Lake Ohrid LOVECLIM simulation data and sedimentary paleoclimate and paleoenvironment proxies. (a) Simulated surface-air temperature (SAT) for the Lake Ohrid grid cell from the LOVECLIM simulation; **(b)** simulated precipitation amount for the Lake Ohrid grid cell from the LOVECLIM simulation; **(c)** Lake Ohrid total organic carbon (TOC) concentrations; **(d)** Lake Ohrid $\delta^{13}C$ endogenic calcite in ‰ relative to VPDB; **(e)** Lake Ohrid $\delta^{18}O$ endogenic calcite in ‰ relative to VPDB; **(f)** Lake Ohrid relative sedimentary quartz content; **(g)** Lake Ohrid K intensities in kilo counts and displayed using a 11pt running mean; **(h)** Lake Ohrid ratio of Ca/K intensities displayed using a 11 pt running mean; **(i)** Lake Ohrid Ca intensities in kilo counts and displayed using a 11 pt running mean; **(k)** Lake Ohrid total inorganic carbon (TIC) concentrations; **(l)** Lake Ohrid deciduous oaks pollen percentages; **(m)** Lake Ohrid arboreal pollen excluding *Pinus* pollen (AP-P)

percentages; red and white diamonds indicate the position of radiometrically dated tephra layers, blue and white diamonds the position of reversals of Earth's magnetic field in the Lake Ohrid sediment record. (b), (d), (e), (K), (l) and (m) are from Fig. 2.

Extended Data Figure 4 | Data analysis. Continuous wavelet transform results for percentages of total inorganic carbon (TIC; **a**) and deciduous oak pollen **(b)** time series from Ohrid DEEP where colour represents the signal amplitude at a given time and spectral period (yellow highest, red lowest power). Black contour is the 5% significance level (chi-squared test according to [81]) against a red-noise background spectrum with autocorrelation coefficient of 0.95, estimated through an autoregressive–moving-average (ARMA) model implemented in PAST ([80] based on [83]). Thick grey line indicates the "cone of influence" outside of which boundary effects can influence the results. Least squares regression (red line) between band pass-filtered 18-25 ky component of **(c)** % TIC and **(d)** the % deciduous oak against precession at 1 ky resolution. Blue lines indicate 95% bootstrapped (n=1999) confidence intervals. Results show significant negative relationships for both proxies, with a stronger response (steeper slope) of the deciduous oaks. Partial least squares regression (PLSR) using TIC and deciduous oaks as predictive variables and LOVECLIM **(e)** temperature and **(f)** precipitation output data as observations. PLSR was performed using SIMCA 14 (Sartorius Stedim Biotech). All datasets were filtered using a frequency centred at 0.05 and a bandwidth of 0.02 prior to multivariate statistical analysis to accommodate for slight offsets in age differences between proxy and simulation data. Results show highly significant positive correlations of simulated temperatures (e) and of simulated precipitation (f) data to proxy data, with a higher sensitivity of TIC and deciduous oaks towards changes in precipitation compared to temperature.

Extended Data Figure 5 | Lake Ohrid precipitation indicators and global monsoon records during MIS 5. (a) Ages of sapropels and humid phases in the Eastern Mediterranean based on Soreq Cave speleothem $\delta^{18}O$ data and U/Th chronology[84]; **(b)** simulated precipitation amount for the Lake Ohrid grid cell from the LOVECLIM simulation; **(c)** Lake Ohrid deciduous oaks pollen percentage; **(d)** Lake Ohrid total inorganic carbon (TIC) concentrations; **(e)** Chinese Speleostack $\delta^{18}O$ [25] in ‰ relative to VPDB; red and white diamonds indicate the position of radiometrically dated tephra layers in the Lake Ohrid record. The chronology of the MIS 5 interval in the Lake Ohrid DEEP site record is based on [85].

Extended Data Figure 6 | Simulated Lake Ohrid precipitation for full-forcing run and sensitivity simulations. (a) Lake Ohrid precipitation (cm yr^{-1}) for full-forcing simulation (black) and a simulation using only orbital forcing under a warm background climate (red). **(b)** Black line as in (a) and a simulation using only orbital forcing under a cold background climate (blue). **(c)** Black line as in (a) and a simulation using full-forcing except for a constant preindustrial NH ice sheet. **(d)** Black line as in (a) and a simulation using full-forcing except for constant preindustrial GHG concentrations. Please note that the sensitivity simulations only cover the last 408 kyr. Please see Methods for details on the sensitivity simulations.

Extended Data Figure 7 | NOAA reanalysis data for the Mediterranean region. (a) Reconstructed precipitation (cm yr^{-1}) for the Lake Ohrid reanalysis grid cell. Data based on monthly means. Dashed line indicates two standard deviations above the mean. **(b)** Composite anomalies of 850 hPa geopotential height (m) associated with Lake Ohrid precipitation maxima shown in (a) and referring to the months shown in (c). **(c)** Monthly distribution of precipitation maxima shown in (a).

Extended Data Figure 8 |. Mean seasonal cycle of Lake Ohrid precipitation - model simulation and NOAA reanalysis data. (a) Mean seasonal cycle of simulated Lake Ohrid precipitation (cm yr^{-1}) for all model years (green) and model years with annual-mean precipitation exceeding two standard deviations (magenta). Please see also Fig. 3a. **(b)** Mean seasonal cycle of Lake Ohrid precipitation (cm yr^{-1}) derived from NOAA reanalysis data (blue) and simulated for the 1–0 kyr period (red). The annual means were removed for better comparison and are provided in the panel.

Extended Data Table 1 | Selected tephra layers from Lake Ohrid and their correlation with tephra layers of other records. $^{40}Ar/^{39}Ar$ ages from literature were recalculated using a decay constant[73] and Alder Creek sanidine (ACs-2) at 1.1891 Ma[74] or Fish Canyon sanidine (FCs) at 28.294 Ma[73]. Tephra ages in bold are used for age-depth modelling in Fig. 1. Age uncertainties are provided according to the original reference (Reference age).

Extended Data Table 2 | Average compositions of OH-DP-2669 and OH-DP-2898 and potential equivalent correlations. Data of SUL2-1, SUL2-22, SUL2-23, SUL2-27 from [51]; SC1-35.50 from [50]; V5, V4, V3, Pitagora ash from [52] and the Parmenide ash from [54]. $\bar{x}$ = mean; S = standard deviation; n= number of analysis.

Fig. 1

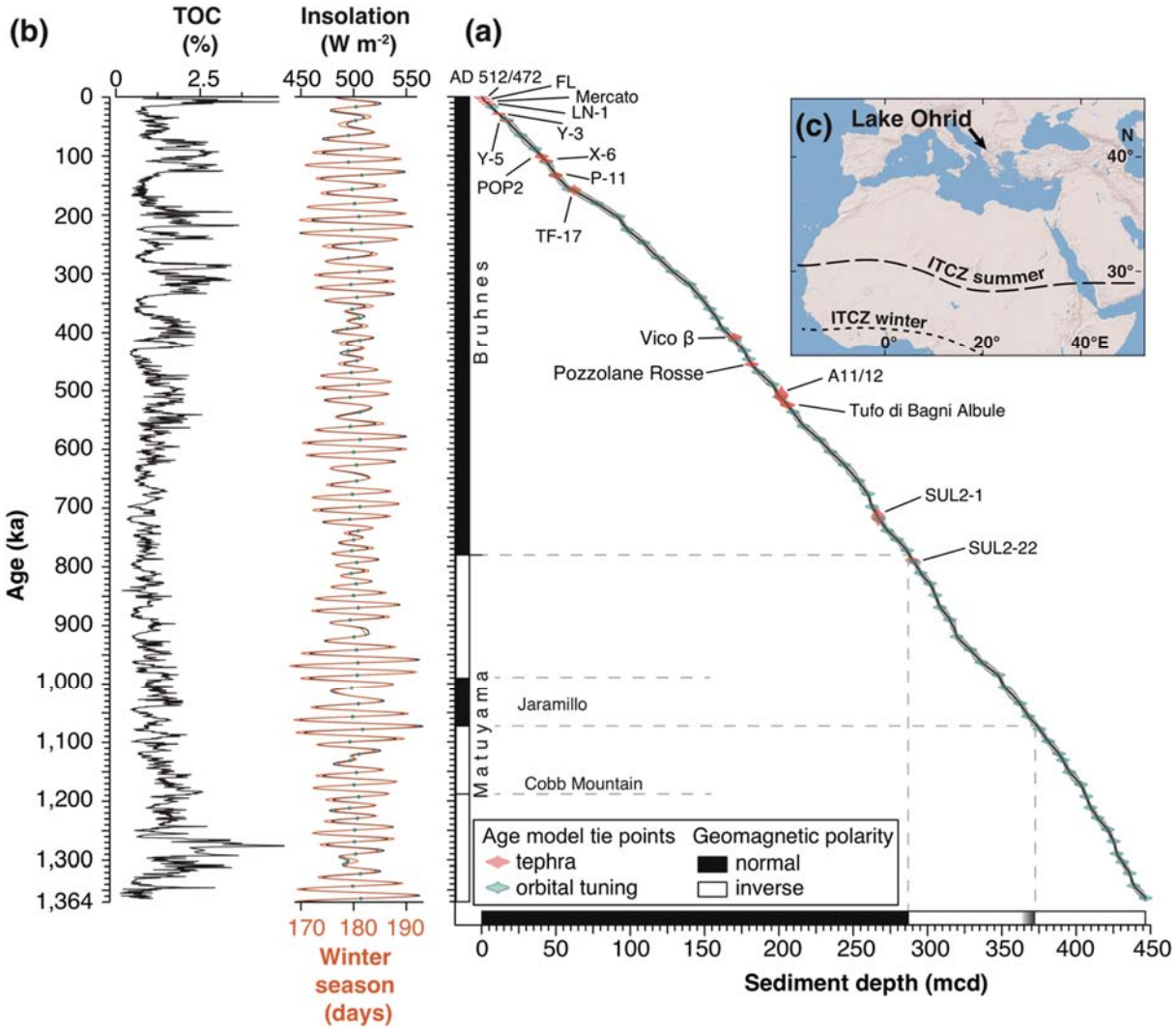
(b)
TOC (%)
Insolation (W m-2)
(a)
(c) Lake Ohrid
ITCZ summer
ITCZ winter
Age (ka)
Winter season (days)
Sediment depth (mcd)
Bruhnes
Matuyama
Jaramillo
Cobb Mountain
AD 512/472
FL
Mercato
LN-1
Y-3
Y-5
X-6
POP2
P-11
TF-17
Vico β
Pozzolane Rosse
A11/12
Tufo di Bagni Albule
SUL2-1
SUL2-22
Age model tie points
tephra
orbital tuning
Geomagnetic polarity
normal
inverse

990 **Fig. 2**
991

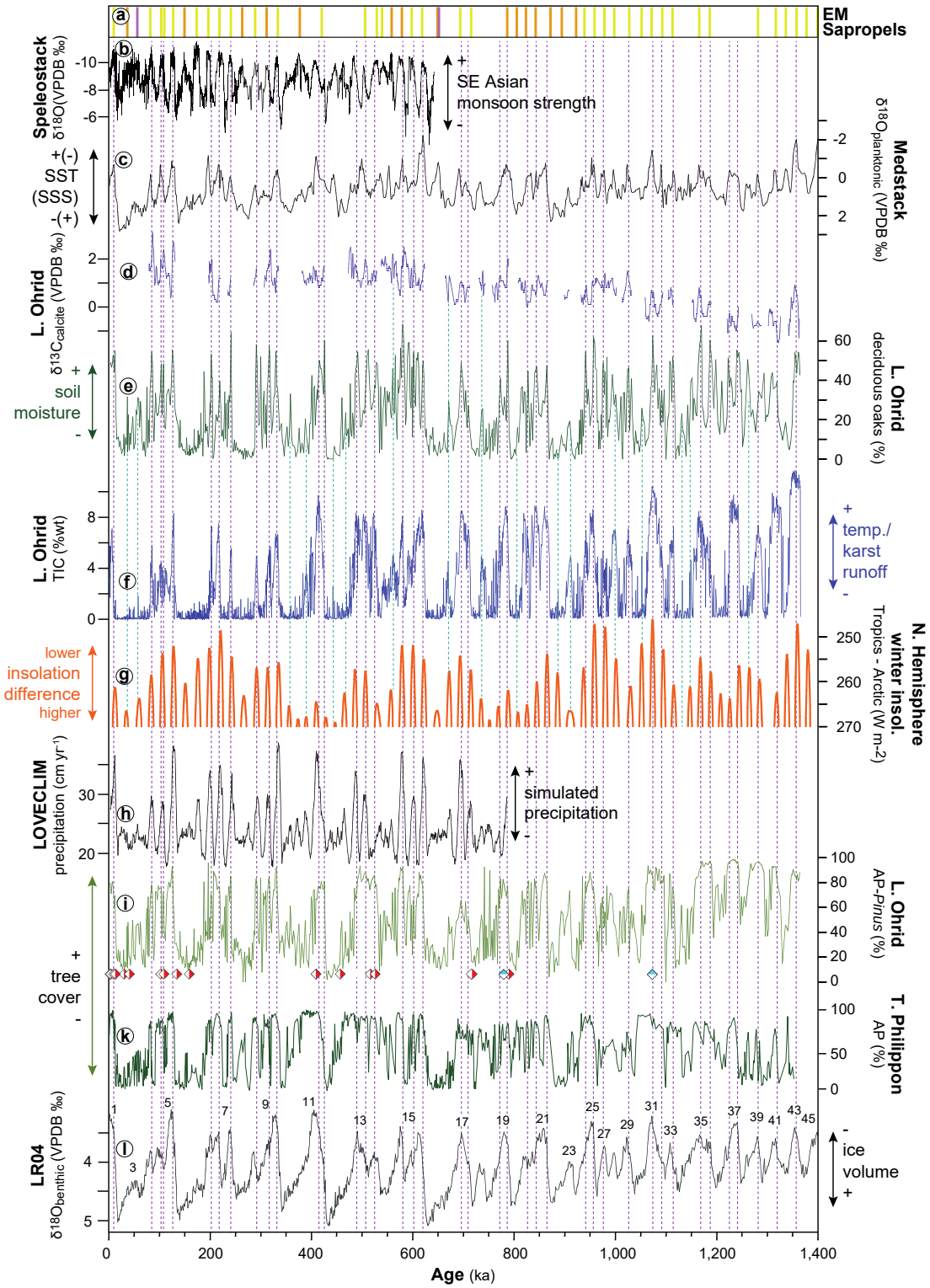

992
993
994

Fig. 3

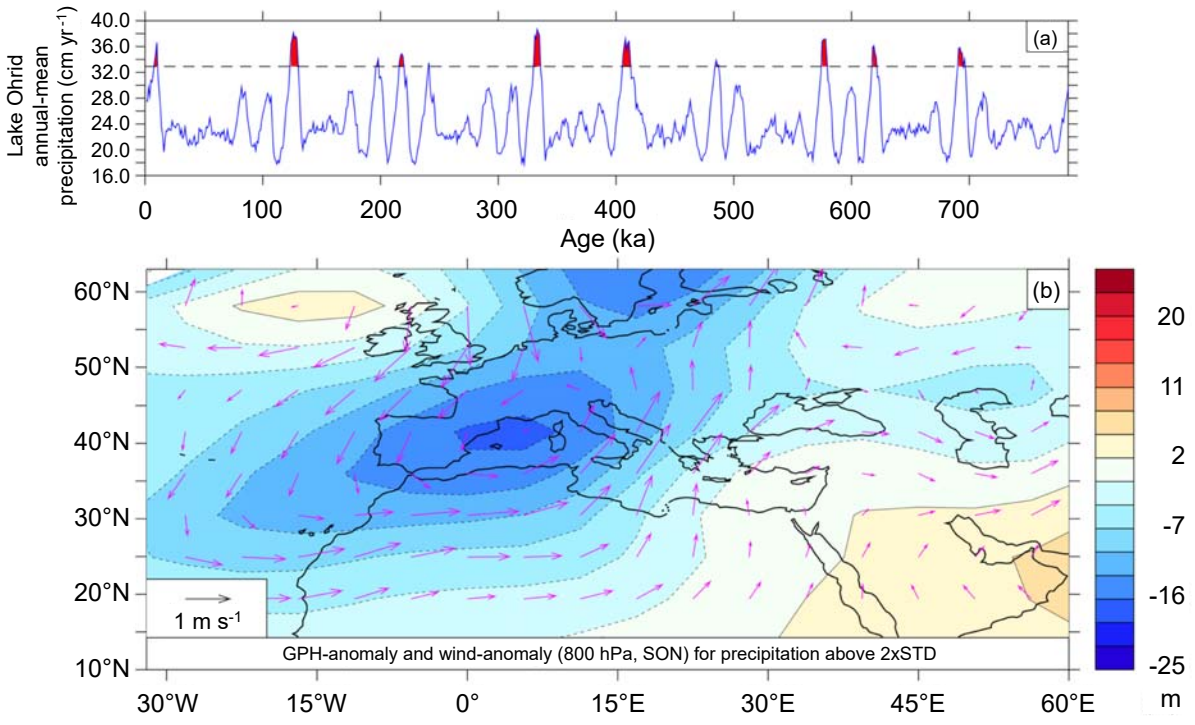
Lake Ohrid annual-mean precipitation (cm yr-1)
40.0
36.0
32.0
28.0
24.0
20.0
16.0
(a)
0
100
200
300
400
500
600
700
Age (ka)
60°N
50°N
40°N
30°N
20°N
10°N
(b)
1 m s-1
GPH-anomaly and wind-anomaly (800 hPa, SON) for precipitation above 2xSTD
20
11
2
-7
-16
-25
m
30°W
15°W
0°
15°E
30°E
45°E
60°E